

Towards Realistic Nonstationarity of Semidiurnal Baroclinic Tides in a Hydrodynamic Model

Arin D. Nelson¹, Brian K. Arbic¹, Edward D. Zaron², Anna C. Savage^{3,4},
James G. Richman⁵, Maarten C. Buijsman⁶, Jay F. Shriver⁷

¹Department of Earth and Environmental Sciences, University of Michigan, Ann Arbor, Michigan, USA

²Department of Civil and Environmental Engineering, Portland State University, Portland, Oregon, USA

³Applied Physics Program, University of Michigan, Ann Arbor, Michigan, USA

⁴Scripps Institution of Oceanography, University of California, San Diego, La Jolla, CA, USA

⁵Center for Oceanic-Atmospheric Prediction Studies, Florida State University, Tallahassee, Florida, USA

⁶Division of Marine Sciences, University of Southern Mississippi, Hattiesburg, Mississippi, USA

⁷Oceanography Division, Naval Research Laboratory, Stennis Space Center, Mississippi, USA

Key Points:

- Hydrodynamic models incorporating mesoscale dynamics and tides are beginning to resolve stationary and nonstationary baroclinic tides.
- The ratio of nonstationary to total semidiurnal variance computed from altimetry and a HyCOM simulation agree at low and middle latitudes.
- Comparisons of analysis methodologies show that the total and nonstationary semidiurnal variances are underestimated in altimetry on average.

This is the author manuscript accepted for publication and has undergone full peer review but has not been through the copyediting, typesetting, pagination and proofreading process, which

may lead to differences between this version and the Version of Record. Please cite this article

as doi: [10.1029/2018JC014737](https://doi.org/10.1029/2018JC014737)

Abstract

Semidiurnal baroclinic tide sea surface height (SSH) variance and semidiurnal nonstationary variance fraction (SNVF) are compared between a hydrodynamic model and altimetry for the low- to mid-latitude global ocean. Tidal frequencies are aliased by the ~ 10 -day altimeter sampling, which makes it impossible to unambiguously identify nonstationary tidal signals from the observations. In order to better understand altimeter sampling artifacts, the model was analyzed using its native hourly outputs and by subsampling it in the same manner as altimeters. Different estimates of the semidiurnal nonstationary and total SSH variance are obtained with the model depending on whether they are identified in the frequency domain or wavenumber domain, and depending on the temporal sampling of the model output. Five sources of ambiguity in the interpretation of the altimetry are identified and briefly discussed. When the model and altimetry are analyzed in the same manner, they display qualitatively similar spatial patterns of semidiurnal baroclinic tides. The SNVF typically correlates above 80% at all latitudes between the different analysis methods, and above 60% between the model and altimetry. The choice of analysis methodology was found to have a profound effect on estimates of the semidiurnal baroclinic SSH variance with the wavenumber-domain methodology underestimating the semidiurnal nonstationary and total SSH variances by 68% and by 66% respectively. These results produce a SNVF estimate from altimetry that is biased low by a factor of 0.92. This bias is primarily a consequence of the ambiguity in the separation of tidal and mesoscale signals in the wavenumber domain.

1 Introduction

The identification and removal of the internal tide sea surface height (SSH) signal is a first-order problem in satellite altimetry. Compared to the relatively large-scale barotropic tides, baroclinic tides (also called internal tides) have a small SSH amplitude (order of cm), are spatially short (order of 100 km) and are significantly affected by ocean stratification and mesoscale currents, making them intrinsically difficult to both discern in altimetry observations and to predict with hydrodynamic models. However, the removal of baroclinic tides from altimetry is critical for distinguishing non-tidal phenomena, and ocean models are increasingly becoming an essential tool in this endeavor. The removal of internal tides will be especially important for the Surface Water and Ocean Topography (SWOT) wide-swath altimeter mission planned to launch in 2021 (Fu, Alsdorf, Morrow, Rodrigues, & Mognard, 2012), which will perform measurements at smaller length scales than any previous altimeter mission.

Currently, baroclinic tides are included in several models such as the Hybrid Coordinate Ocean Model (HyCOM) (B. Arbic et al., 2018; B. K. Arbic, Richman, Timko, Metzger, & Wallcraft, 2012; B. K. Arbic, Wallcraft, & Metzger, 2010), the MIT General Circulation Model (MITgcm) (e.g., Rocha, Chereskin, Gille, and Menemenlis (2016); Rocha, Gille, Chereskin, and Menemenlis (2016)), the German STORMTIDE model (e.g., Müller, Cherniawsky, Foreman, and von Storch (2012)), the Nucleus for European Modeling of the Ocean (NEMO) community model (Madec, 2008), and the Geophysical Fluid Dynamics Laboratory (GFDL) Generalized Ocean Layered Dynamics model (GOLD) (e.g., Waterhouse et al. (2014)). Some regional baroclinic tide models exist as well (e.g., Kelly, Lermusiaux, Duda, and Haley (2016)). In fact, it is only recently that computing power has progressed enough to feasibly allow global ocean models to run at the high spatial and temporal resolutions necessary to resolve baroclinic tides.

Baroclinic tides are created when barotropic tidal currents pass over sloping topography, generating internal waves that are phase-locked with the tidal forcing (Kelly, Nash, & Kunze, 2010). These phase-locked internal waves are referred to as stationary tides since they can be written in terms of a known amplitude and phase and are hence predictable. Internal tides may lose their phase relationship with the barotropic forcing as they interact with topography (e.g., Duda et al. (2012); Kly-

mak et al. (2016)), as they propagate through time-variable ocean stratification (e.g., Buijsman et al. (2017)), or by interacting with sub-tidal flows including eddies and currents (e.g., Dunphy and Lamb (2014); Dunphy, Ponte, Klein, and Le Gentil (2017); Kelly and Lermusiaux (2016)). These are called nonstationary tides, and they are less predictable by nature. Hydrodynamic models that are able to simulate internal tides along with mesoscale and submesoscale dynamics should also simulate nonstationary internal tides, meaning it may be possible for them to aid in predicting nonstationary tides for future altimetry missions. Motivated by this, the percent variance of the semidiurnal (twice-daily) internal tides that is nonstationary in a hydrodynamic model will be computed in this paper and compared with the same quantity computed from altimetry.

Although their temporal resolution is relatively coarse, altimeter observations have been used to study global baroclinic tides (Ray & Mitchum, 1996, 1997; Ray & Zaron, 2016; Zhao, Alford, Girton, Rainville, & Simmons, 2016). With a temporal resolution on the order of 10 days, altimeters alias the tides and other high-frequency motions onto lower frequencies. To circumvent the issue of aliasing, tidal analyses using altimetry are often performed in the wavenumber domain. The differences caused by the choice of analysis in either the frequency or wavenumber domain has not yet been quantified in the context of ocean tides. In this work, we use both methodologies to analyze model output with a sufficiently high temporal resolution to investigate this quandary.

Several studies exist where altimeter observations are used to gauge the fidelity of global simulations containing baroclinic tides (Ansong et al., 2015; B. K. Arbic et al., 2012; Müller et al., 2012; Shriver et al., 2012), of which all but Müller et al. (2012) focused on HyCOM. These studies found that the spatial averages of stationary tidal amplitudes in HyCOM agreed well with observations in ‘hot-spot’ regions of large internal tide generation, but did not agree as well in regions of strong mesoscale activity and/or small tidal amplitudes (Shriver et al., 2012). This study goes one step further by comparing the nonstationary tidal amplitudes and semidiurnal nonstationarity variance fraction (SNVF) on basin- and global scales.

No matter if the analysis is done in the frequency or wavenumber domain, SNVF is determined by computing the spectra before and after the stationary tides have been subtracted from the time series, integrating over the semidiurnal internal tide frequency or wavenumber band, then computing the ratio of the nonstationary to total semidiurnal variance. This procedure for computing SNVF is relatively easy to perform in the frequency domain since the tides and other physical features (e.g. mesoscale eddies) have clearly separate time scales. However, in the wavenumber domain, internal tides and mesoscale eddies have similar length scales, and there is ambiguity in how to separate these signals. This leads to a number of subjective choices that will be identified and discussed. The model is sufficiently resolved to use both methodologies, allowing for the identification of limitations and biases in the wavenumber domain methodology. Implications of these limitations and biases for past and future altimetry missions will be briefly explored.

2 Data and Methods

The objective of this paper is to assess the nonstationary tides within a state-of-the-art ocean model by comparing them with data available from satellite altimetry. By definition, the nonstationary tide refers to a signal that originates from the tide generating force but is not phase-locked to this forcing. This definition corresponds most logically with an analysis method that first identifies the stationary tide by harmonic analysis – identifying the signal component that is phase-locked to the tidal forcing – and then identifies the residual signal within a given frequency bandwidth around the known tidal frequencies. Thus, the identification of the nonstationary tide is most naturally accomplished in the frequency domain. While it is feasible to

125 analyze the tides in the hourly output of a numerical model using this methodology
126 (Buijsman et al., 2017; Savage et al., 2017), which shall be referred to as the “ f -
127 space” (frequency-space) methodology, it is not feasible to apply this to altimeter data.
128 Various approaches have been employed to identify nonstationary tides from altimetry,
129 but ambiguity is introduced by the limitations inherent in the sampling of altimeters
130 which alias the tidal frequencies (Zaron, 2015, 2017; Zhou, Wang, & Chen, 2015). The
131 method used in this paper shall be referred to as the “ k -space” (wavenumber-space)
132 methodology, since it infers the nonstationary tide from the wavenumber spectrum,
133 rather than the frequency spectrum.

134 In this section the k -space methodology that was originally used with altimetry
135 is described in detail. The key to the comparison of model and data in this study is
136 to use the k -space methodology on the model output, after subsampling to match the
137 altimetry. Additionally, though, the native-resolution model output permits the sepa-
138 rate comparison of the k -space and f -space methodologies, solely from model output,
139 in order to identify likely errors and biases in the k -space approach – a comparison
140 which is not possible from analysis of altimeter data alone.

141 2.1 Altimetry

142 The altimeter data and analysis methodologies used in this study come from
143 Zaron (2017). The data consists of the combined 23 years of TOPEX/Poseidon, Jason-
144 1, and Jason-2 (T/P-J) altimeter measurements with all standard corrections applied,
145 including environmental path delays, the inverse barometer effect, sea-state bias, mean
146 sea level, solid earth tides, and barotropic tides. From these data, 2,000 km long
147 track segments centered at each ascending and descending track cross-over point were
148 collected. For data near land, tracks shorter than 1,200 km or with gaps greater than
149 30 km were rejected.

150 The orbit repeat time of the T/P-J altimeters is 856712 seconds (9.91565 days)
151 on average (Benada, 1997). Because of this, traditional f -space analyses cannot easily
152 distinguish tidal motions in altimeter data since all sources of variability with fre-
153 quencies shorter than half the altimeter sampling frequency will be aliased onto lower
154 frequencies. This orbit repeat time was chosen so that tidal aliases would not overlap
155 with significant periods of climate variability such as the seasonal cycle, annual cycle,
156 or longer periods. Even so, tens or sometimes even hundreds of altimeter passes are
157 needed to reliably separate tidal variability from other motions (see, for example, the
158 tidal aliasing periods associated with the T/P-J missions in Table 3 of Ray (1998)).
159 Therefore, the along-track analysis of internal tides from altimetry is typically per-
160 formed in k -space. The k -space analysis method of Zaron (2017), which is based upon
161 methods in Ray and Zaron (2011), will be summarized here.

162 First, an estimate of non-tidal variability was subtracted from the SSH anomaly
163 relative to the record-length mean SSH to reduce the amount of non-tidal mesoscale
164 variability. This “mesoscale correction” was performed by subtracting the SSH fields
165 from the Archiving, Validation, and Interpretation of Satellite Oceanographic Data
166 (AVISO) center’s Data Unification and Altimeter Combination System (DUACS) ver-
167 sion DT-2014 (Pujol et al., 2016). This mesoscale correction was also used in Ray
168 and Zaron (2016) and Zaron (2017), although it has been noted that there is some
169 leakage of internal tide variability in this AVISO data (Zaron and Ray (2018); also
170 see the Appendix of Ray and Zaron (2016)). Even with this contamination, this
171 mesoscale correction was found to be essential for identifying internal tidal signals in
172 the temporally-aliased altimeter data.

173 From this “corrected” data, the stationary tide was identified and removed from
174 each time series using harmonic analysis. k -space power spectral densities were then
175 computed along each track for each altimeter cycle from both the total and stationary
176 tide-subtracted (or nonstationary) SSH data with Hann windows applied. These spec-
177 tra were then averaged over all cycles. It should also be noted that, contrary to some

178 previous works (e.g., Ray and Zaron (2016)), no high-pass spatial filter was applied
 179 to the along-track data at any point during this analysis. The high-pass filter used
 180 in these works was originally used to remove mesoscale eddies and other larger-scale
 181 features, but it was found to remove some tidal variability as well, hence our choice to
 182 neglect this operation.

183 In Zaron (2017), the SSH k -space spectra were shown to consist mainly of a
 184 broadband continuum besides a bump around the baroclinic wavenumbers and a white-
 185 noise-like spectrum at short wavelengths (≤ 30 km). The noise level was defined by
 186 averaging the k -space spectra beyond this limit, and the broadband continuum was
 187 modeled as a low-order polynomial.

188 The variance associated with the mode-1 semidiurnal internal tides is estimated
 189 by integrating the variance under the spectral bump. The relatively short length of the
 190 along-track segments does not permit resolution of the wavenumber peaks associated
 191 with individual tidal frequencies in the semidiurnal band (e.g., M₂, S₂, N₂, etc.);
 192 therefore, the integrated variance is a sum of all these components. Since the M₂ tide
 193 is generally the largest amplitude, the wavelength of the mode-1 M₂ tide, denoted
 194 k_{M_2} , is used to locate the peak, and variance is computed by integrating between
 195 wavenumbers k_1 and k_2 , $k_1 \leq k_{M_2} \leq k_2$, defined by the local minima in the corrected
 196 spectrum closest to k_{M_2} . The white-noise and broadband variances between these
 197 wavenumbers were also computed and subtracted, resulting in “residual” total and
 198 nonstationary variances. The semidiurnal nonstationary variance fraction (SNVF) was
 199 then computed by dividing the residual nonstationary variance by the residual total
 200 variance. See Figure 1 for an application of this methodology at a single altimeter
 201 cross-over.

202 The distinction between stationary and nonstationary variance is reasonably
 203 straightforward when time-resolved SSH is analyzed in the frequency domain (e.g.,
 204 Colosi and Munk (2006)); however, the above-described methodology involves poten-
 205 tially problematic, and subjective, choices to deal with the altimeter temporal aliasing
 206 and relatively small signal-to-noise level. These choices include the definition of (1)
 207 the white-noise and (2) broadband spectra, (3) the mesoscale correction method, (4)
 208 the choice of integration limits, and (5) how the variance estimates from the ascending
 209 and descending tracks were reconciled into a single value. In order to reproduce the
 210 analysis of Zaron (2017), we had to replicate their choices as closely as possible; these
 211 choices will be discussed in the results. The five subjective choices used by Zaron (2017)
 212 were used when performing the k -space analyses of the model data, with one small
 213 difference; the mesoscale correction for the model was performed by subtracting the
 214 weekly-running mean from every time series, replicating a “perfect” implementation
 215 of the mesoscale correction methodology applied by Zaron (2017).

216 2.2 Model Output

217 This work uses 5 years of hourly steric SSH output from a HyCOM simulation
 218 managed by the Naval Research Laboratory (NRL) run on a tri-polar spatial grid with
 219 a nominal spacing of $1/12.5^\circ$ near the equator. In addition to the standard atmospheric
 220 forcing fields, this simulation included forcing at the four strongest diurnal tides (K₁,
 221 O₁, P₁, Q₁) and the four strongest semidiurnal tides (K₂, M₂, N₂, S₂). Steric SSH
 222 instead of total SSH was used since it doesn't contain barotropic motions. See the
 223 appendix of Savage et al. (2017) for a discussion of the procedure used to compute
 224 steric SSH in HyCOM.

225 The output from this simulation was used in Shriver et al. (2012) and numerous
 226 studies thereafter (Richman, Arbic, Shriver, Metzger, & Wallcraft, 2012; Timko et al.,
 227 2012, 2013). There are newer HyCOM tides simulations having higher spatial resolu-
 228 tion (e.g., $1/25^\circ$ as in Savage et al. (2017)) and more accurate barotropic tides (e.g.,
 229 Ngodok, Souopgui, Wallcraft, Richman, and Shriver (2016)), but the older simulation
 230 was used because of its longer output duration (5 years as opposed to 1 year in other

simulations, including Savage et al. (2017)). The longer output was essential when analyzing the altimeter-sampled model output because altimeter sampling provides only about 72 tracks per cross-over point per year, and longer time series of SSH have been shown to produce better estimates of nonstationarity (Ansong et al., 2017).

Because the output of the HyCOM simulation was saved hourly, it is feasible to compute the tidal statistics using the f -space methodology, defined as integrating the frequency power spectral densities of the total and nonstationary SSH time series between 1.85-2.05 cycles per day (Savage et al., 2017) at the model grid point closest to the respective altimeter cross-over point. However, it is important to process and analyze the model output in the same fashion as the observations in order to obtain the most reasonable comparison between the two. In this case, the hourly model output was sampled using the spatial pattern of sampling along the T/P-J tracks (Benada, 1997). Additionally, having both hourly and altimeter-cycle time series allows us to compute the tidal statistics using three possible methodologies:

1. k -space of the altimeter tracks sampled once per altimeter cycle,
2. k -space of the hourly altimeter tracks, and
3. f -space of the hourly time series averaged over all altimeter points.

The first analysis is the best analogue to that used in the observations, so the results of this analysis are the best choice for comparing the model output to the observations. The second analysis will be used to investigate how the temporal sampling of the altimeters affect the k -space results. The last analysis will be used to investigate possible biases in using the k -space methodology in place of the f -space methodology when both methodologies are feasible.

3 Results

3.1 Analyses at a Single Location

To validate our analysis procedures, we applied them to altimeter-sampled HyCOM tracks corresponding to the six regional analyses defined in Section 4 of Zaron (2017). These locations have varying strengths of mesoscale variability, stationary tides, and nonstationary tides. For brevity, the results of only one test location will be shown here; the cross-over point located at 10°S, 3°W in the Southeast Atlantic. This location was chosen for this discussion since it contains moderate strengths of both tidal and non-tidal variability. The results of these analyses are displayed in Figure 1. The five subjective choices in the k -space methodology listed at the end of Section 2.1 will now be discussed:

1. Noise removal. Zaron (2017) and others have noted the presence of a pervasive white-noise spectrum that can be characterized using the high-wavenumber portion of the spectrum. For this work, the white-noise region was defined akin to Zaron (2017) at wavelengths lower than 30 km. Since this white-noise spectrum is subtracted from the full spectrum, the subjective choice of how to define the white-noise spectrum could affect the later variance estimates. The noise is generally much smaller than the variances of interest in the altimeter data and is almost non-existent in the model, so the results are the least sensitive to this choice amongst the five.
2. Broadband removal. The broadband spectrum differs greatly with location (see, e.g. Figure 2 of Zaron (2017)). Additionally, the mesoscale correction can significantly affect the shape of the broadband spectrum. This makes it tricky to choose a satisfactory global definition for the broadband spectrum. In this work, an order-2 polynomial was chosen to account for any curvature in the broadband while limiting any overfitting that could occur when using higher-order polynomials.

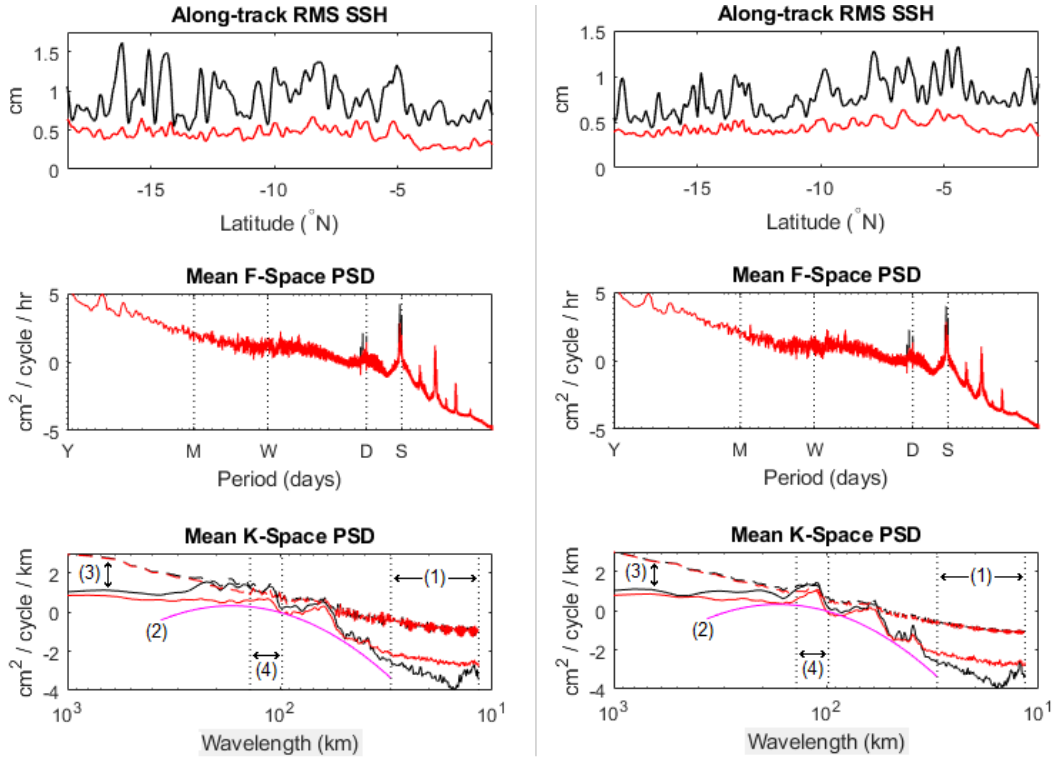


Figure 1. Along-track analysis of the altimeter-sampled HyCOM output from the South-east Atlantic centered on 10°S , 3°W for the (left) ascending track and (right) descending track. (Top) Total (black) and nonstationary (red) semidiurnal root-mean-square SSH values at each point along each track. (Middle) Mean f -space power spectral density from each model output hourly time series along each track. Vertical dotted lines are plotted at yearly (Y), monthly (M), weekly (W), diurnal (D), and semidiurnal (D) frequencies. (Bottom) Mean k -space power spectral density from each altimeter-sampled track, including spectra for the total SSH (black), the nonstationary SSH (red), and the broadband model (magenta). The dashed lines are the spectra when the mesoscale / non-tidal variability is not removed. The four numbers/regions label the first four of the five subjective choices of the k -space analysis method listed in the text. The uncertainty of the stationary tidal fit causes the increase in variance in the low wavenumbers of the nonstationary SSH spectrum relative to the total SSH spectrum.

- 281 3. Mesoscale / non-tidal variability removal. The choice of mesoscale model to re-
 282 move non-tidal variability from altimeter-sampled results is another complexity.
 283 As has been shown, even utilizing an imperfect mesoscale model is important
 284 in clearly identifying the stationary internal tides (e.g., Ray and Zaron (2016)).
 285 For the altimeter-sampled model output, a weekly-running-average was sub-
 286 tracted from all time series to mimic a “perfect” mesoscale model following the
 287 characteristics of the mesoscale model used in Zaron (2017).
- 288 4. Choice of integration limits. At many locations, the local stationary tide is a
 289 sum of propagating stationary tidal waves from multiple sources. If the tides
 290 propagate at a high angle relative to the altimeter track (see, e.g., Figure 6
 291 in Ray and Zaron (2016)), there may be multiple peaks in the wavenumber
 292 spectrum that may or may not reside within the integration limits of the mode-
 293 1 wavenumber k_{M2} . For example, the bottom subplot in Figure 1 show multiple

294 peaks beyond 100 km in the total SSH spectrum but not the nonstationary SSH.
 295 This indicates that there are sources of nonstationary tides propagating at large
 296 angles relative to the altimeter track, which manifests as variance at wavelengths
 297 beyond the k_{M2} band as defined in this work. Following previous works, the
 298 integration limits were chosen to be the local minima surrounding only the peak
 299 in the wavenumber spectrum closest to k_{M2} , meaning the semidiurnal variances
 300 at some locations may be grossly underestimated.

301 5. Reconciling results from the two tracks. In this work, the variance estimates
 302 from the ascending track and descending track are averaged to give a single
 303 value for the variance at each cross-over point. As mentioned in the discussion
 304 of the choice of integration limits, the k -space spectrum from the descending
 305 track contains a majority of its stationary semidiurnal variance between the
 306 local minima surrounding the peak nearest the k_{M2} peak, while ascending track
 307 k -space spectrum contains a significant amount of variance outside the k_{M2}
 308 integration limit at longer wavelengths. Since the variance estimates from the
 309 two tracks are averaged, the missing variance in the ascending track's variance
 310 estimate constitutes an as-of-yet unresolved error in the concluding variance
 311 estimate at this cross-over location.

312 3.2 Semidiurnal Variances and Variance Ratios

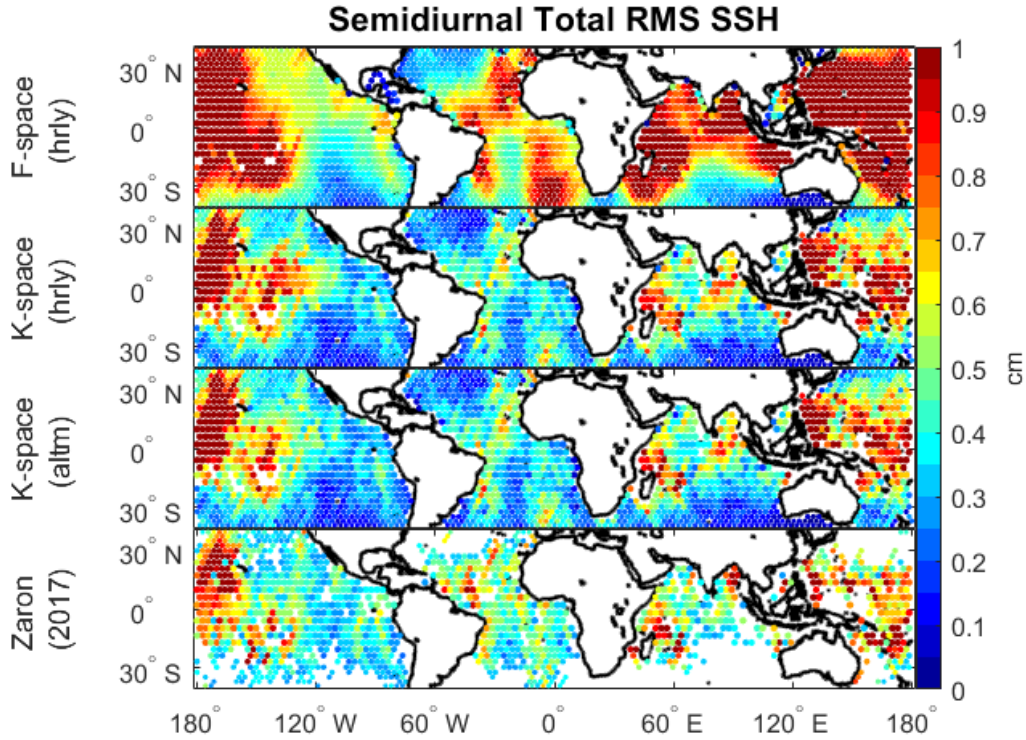


Figure 2. Global maps of semidiurnal total SSH variability (root-mean-square anomaly). The top three maps are computed from the HyCOM 1/12.5° 5-year run using (top) f -space methodology applied to the hourly output, (second) k -space methodology applied to the hourly output, and (third) k -space methodology applied to the altimeter-sampled output. These are plotted alongside (bottom) the results from altimetry in Zaron (2017). In all subplots, results are only plotted where the id=EDZtotal semidiurnal variance σ_T^2 is greater than twice the error variance σ_E^2 .

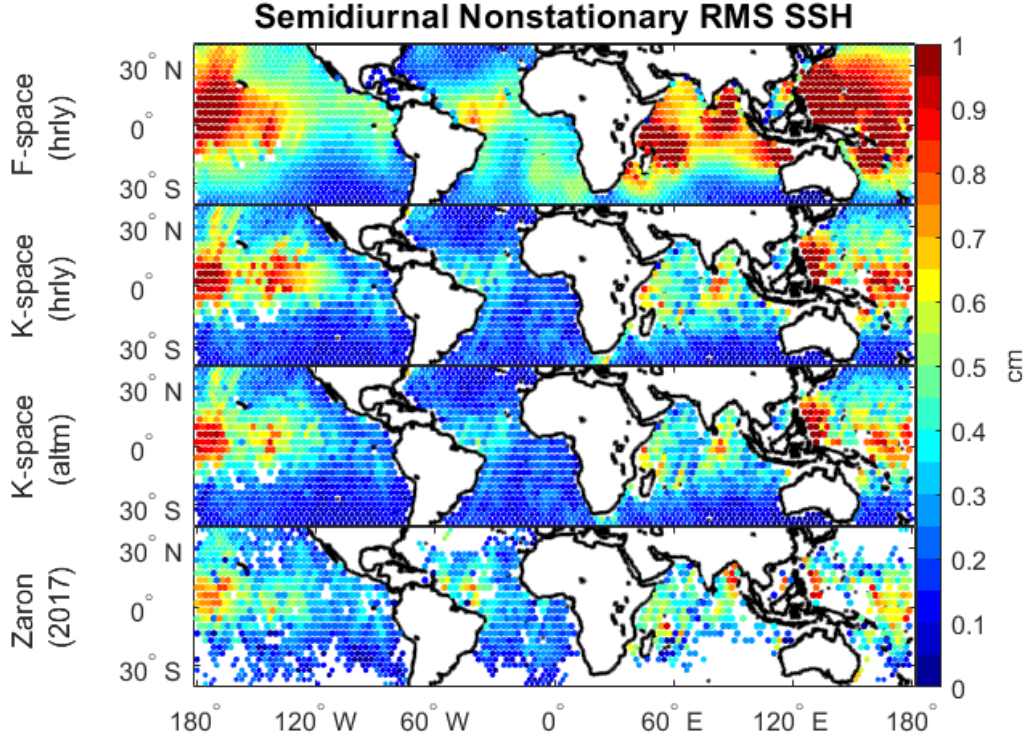


Figure 3. As in Figure 2, but for semidiurnal nonstationary SSH variability.

313 Figures 2 to 4 display global maps of the total and nonstationary semidiurnal-
 314 band SSH variabilities and SNVF for the three different methodologies listed in Section
 315 2.2 along with the results from altimetry in Zaron (2017). At a cursory glance, all
 316 analyses show similar qualitative features. In the maps of nonstationary semidiurnal
 317 SSH variability (Figure 3), there is a large band of nonstationarity in the equatorial
 318 Pacific Ocean, due to the equatorial crossings of the stationary tides generated near
 319 Hawaii, near the Philippines, and in the tropical south and southwest Pacific. This
 320 is consistent with the analysis of the HyCOM simulation studied by Buijsman et
 321 al. (2017). There is additionally a large amount of nonstationarity in the Indian
 322 Ocean where the stationary tides generated near Madagascar cross the Mascarene
 323 Plateau, the Chagos-Laccadive Ridge, and the Ninety East Ridge as they propagate
 324 further eastward. There is also strong nonstationarity in regions of high mesoscale
 325 variability (e.g. boundary currents), where the mesoscale dynamical features (e.g.
 326 eddies) refract and scatter the internal tide. Additionally, as also found in Zaron
 327 (2017), low semidiurnal tidal variances and high observational uncertainties polewards
 328 of 40° caused the analysis to be restricted to equatorwards of 40° . In all figures, data
 329 are only plotted where the $[id=EDZ]_{total}$ semidiurnal variance σ_T^2 is greater than twice
 330 the error variance σ_E^2 error variance σ_E^2 is less than twice the total semidiurnal variance
 331 σ_T^2 . In the model, this error is almost zero.

332 The major discrepancy in these results is that the k -space method tends to
 333 underestimate both nonstationary and total semidiurnal variances. Conversely, the k -
 334 space method differs marginally when applied to 10-day sampled model output versus
 335 the original hourly output of the model, which is unsurprising as the altimeter repeat
 336 time was chosen specifically to minimize the temporal aliasing on the tides, and a three-
 337 year span was found to be satisfactory for capturing semidiurnal stationary tides (Ray
 338 & Zaron, 2011). The discrepancy in the f -space and k -space results stems from a
 339 combination of the five subjective parameters in the k -space method listed previously,
 340 the effects of which vary strongly with location. The ratio global area-weighted average

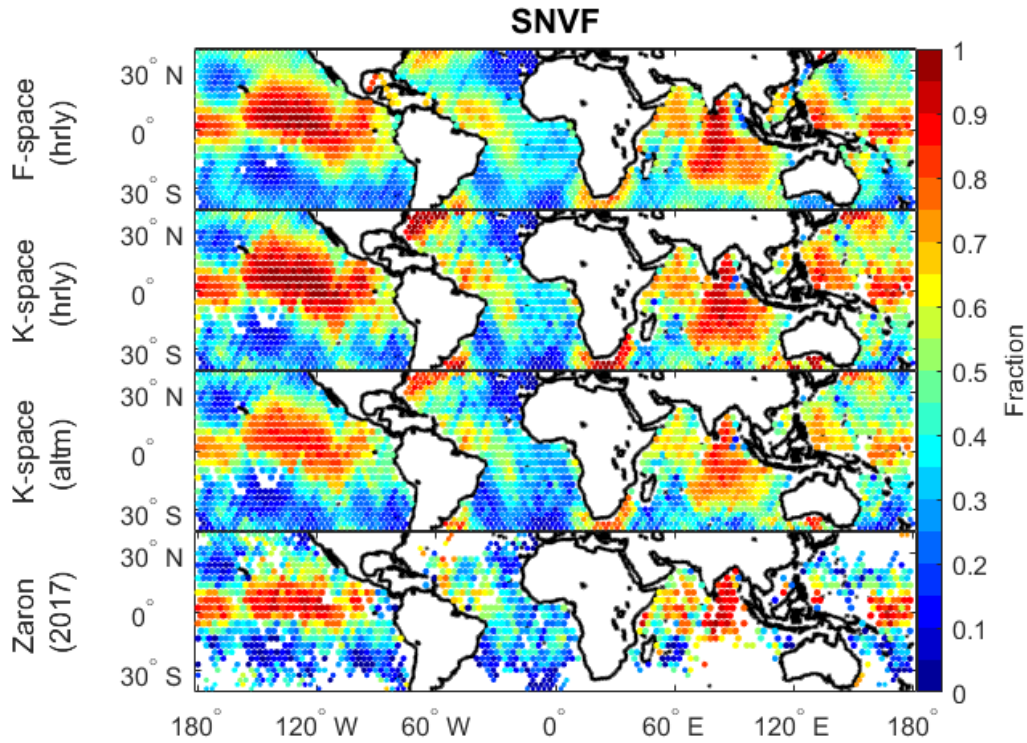


Figure 4. As in Figure 2, but for SNVF.

of the nonstationary semidiurnal variance from the k -space methodology (0.12 cm^2) versus that from the f -space methodology (0.37 cm^2) is 0.32. For the total semidiurnal variance, the ratio of the k -space estimate (0.26 cm^2) to the f -space estimate (0.77 cm^2) is 0.34. This highlights the importance of processing and analyzing observational data and model outputs as similarly as possible for the comparisons between the two to be meaningful. If the f -space methodology applied to the hourly data (e.g. this work, or the results of Savage et al. (2017)) were compared directly to altimetry, the model would appear to be grossly overestimating semidiurnal baroclinic variances, especially in the Indian Ocean and central and western Pacific Ocean. However, the k -space method applied to the altimeter-sampled model output agrees much better with the altimetry, showing more similar spatial patterns and variance magnitudes, with the model only slightly overestimating the semidiurnal baroclinic variances.

Perhaps most surprising is the similarities in the SNVF across analysis methods. Qualitatively, all three methodologies applied to the model output show very similar spatial patterns and SNVF values, all of which also appear to agree well with the results from altimetry. This robustness in the comparison of the variance ratios versus the individual variances was quantitatively assessed by computing the correlations between the various variances and SNVF across the different methods in 10° latitude bins. These correlations are displayed in Figure 5. All correlations are statistically significant to at least 95% confidence. Across all three comparisons, the SNVF has the highest correlation between analysis methods averaged across all latitudes. For all analysis methods and correlations from the model output, there is no discernible pattern versus latitude.

Between the model output and altimetry, the semidiurnal total SSH variance is consistently correlated versus latitude at 0.5-0.6 in the equatorial ocean and at 0.7-0.8 in the northern midlatitude ocean. Semidiurnal nonstationary SSH variance correlates most well along the equator and lessens as latitude increases polewards. This is due

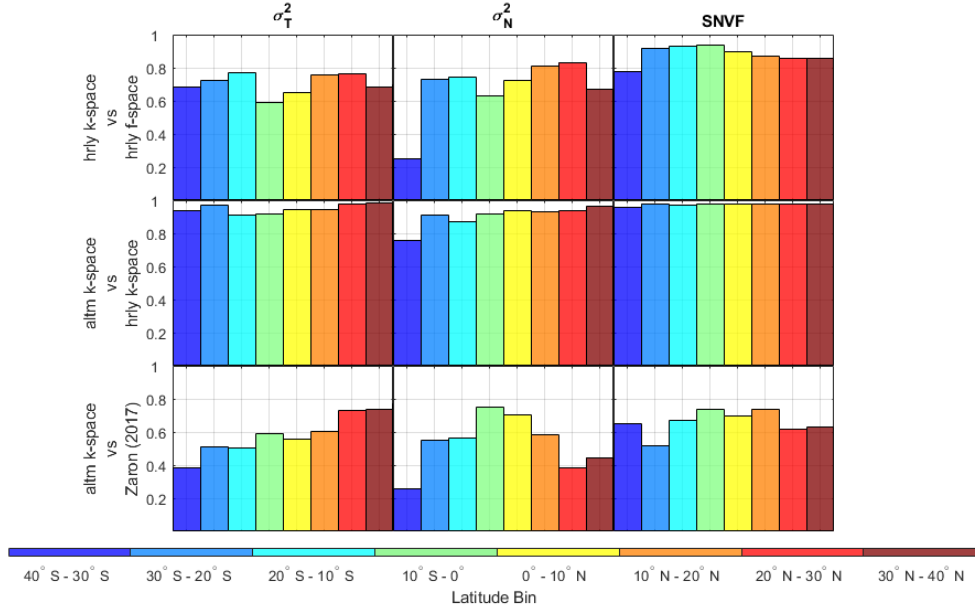


Figure 5. Correlations between the estimates of the semidiurnal variances of the total σ_T^2 and nonstationary σ_N^2 SSH and their ratio, the SNVF, between the three methodologies over 10° latitude bins.

368 to how the nonstationary tides are generated in these two regimes. Stationary tides
 369 propagating across the equator are mainly scattered by the change in ocean stratifica-
 370 tion and equatorial currents (Buijsman et al., 2017), which are relatively broad-scale
 371 and thus well simulated in the model. At higher latitudes, nonstationary tides are pri-
 372 marily generated by dynamical features such as eddies and western boundary currents.
 373 The HyCOM simulation did not include data assimilation, so the locations of these
 374 features, and thus the spatial distribution of the nonstationarity, may be mismatched
 375 relative to what was seen in altimetry. Surprisingly, even with these discrepancies in
 376 the stationary and nonstationary variances, the SNVF ratio stays relatively consistent
 377 across latitudes, although the correlations are slightly higher near the equator.

378 4 Discussion

379 As global ocean models such as HyCOM have attained progressively more realism
 380 through improved resolution and representation of atmospheric and tidal forcing, the
 381 related tasks of calibration and validation have proceeded step-wise, through model-
 382 data intercomparison of separate physical phenomena such as mesoscale kinetic energy
 383 (Thoppil, Richman, & Hogan, 2011), mesoscale available potential energy (Luecke
 384 et al., 2017), tidal SSH variability (Ansong et al., 2015; Shriver et al., 2012) and
 385 others. In this paper, we seek to validate a model’s nonstationary tide, which arises
 386 as a joint phenomenon of the tides and mesoscale dynamics simultaneously. The
 387 motivation for this study is both to understand whether the model’s representation of
 388 the interaction between these phenomena is adequate, and to establish a benchmark of
 389 skill for comparison of future efforts which will likely seek to forecast the nonstationary
 390 tide in the context of the SWOT swath altimeter mission (Fu et al., 2012).

391 A key finding of the present study is the degree to which the wavenumber-space
 392 (k -space) methodology underestimates the nonstationary tidal SSH variance. Assum-
 393 ing the model is accurate enough to be used as a guide, a comparison of the f -space

and k -space methodologies finds that the latter is biased low and misses a large fraction of the nonstationary variance (cf., top two panels of Fig. 3). The k -space methodology was developed to overcome the effects of altimeter aliasing, but its implementation relies on several procedures, the validity of which cannot be tested from altimeter data alone. These procedures include (in order from least to most significant) the estimation and removal of a white-noise instrumental error spectrum, correction for the mesoscale/non-tidal SSH variability, estimation and removal of a broadband mesoscale/non-tidal spectrum, choice of integration limits defining the nonstationary spectrum bandwidth, and accounting for non-isotropy by averaging spectra from ascending and descending tracks. Zaron (2017) highlighted the role played by the assumed broadband mesoscale/non-tidal spectrum and noted that if this broadband spectrum consisted of a steeply sloped spectrum, e.g., k^{-3} , buried “underneath” the tide-dominated spectrum, then the nonstationary variance could be much larger than the values inferred there. Indeed, the present study indicates that this is the case. The ratio of the area-weighted global average of the semidiurnal nonstationary variance obtained with the k -space analysis (0.12 cm^2) with the f -space analysis (0.37 cm^2) is found to be 0.32. For the semidiurnal total variance, ratio of the variance from the k -space analysis (0.26 cm^2) to the f -space analysis (0.77 cm^2) is 0.34. However, the ratio of the area-weighted global average SNVF from the k -space analysis (0.45) to that from the f -space analysis (0.49) is 0.92.

Because the k -space analysis produces biased estimates of both the nonstationary and the total tidal variance, their ratio, the SNVF, is relatively well-correlated between the model and the altimetry (cf., Fig. 5). This positive correlation, and the map of Figure 4, suggest that HyCOM is accurately representing the interactions of the baroclinic tides and mesoscales; however, as the preceding paragraph makes clear, the altimeter data provide relatively weak constraints for describing the nonstationary tide — at least using the data and methods presently in the literature. The challenge with validating a global model such as HyCOM is the tradeoff between temporal- and spatial-resolution inherent in most data sources. Analysis of stationary and nonstationary tides using data from surface drifters is currently being investigated to overcome some of the limitations of altimetry data (Elipot et al., 2016).

5 Summary

In order to compare and validate ocean models results with observed data, it is necessary to implement ocean model analysis procedures that match the procedures used in the observations. This matched approach has been taken on in order to compare the nonstationary tides simulated with a combined tides-and-mesoscale-resolving HyCOM simulation with the nonstationary tides inferred using satellite altimetry. The comparison finds that the steric height variance associated with baroclinic tides is considerably larger in the model than in the data; however, the ratio of nonstationary to total tidal variance, denoted SNVF, is spatially-correlated between the model and data.

These results were rationalized by examining carefully the statistics of the nonstationary tide in different sub-samples of the model output, as they were progressively degraded from the native resolution of the model to the coarser resolution of the altimetry. The notion of nonstationary tidal variance, which is unambiguously defined in the frequency domain, is not clearly defined in the wavenumber domain, and complicates the analysis of altimetry data. Assuming the HyCOM results are accurate enough to be used as a guide, the globally-averaged altimeter-based estimates of the nonstationary and total semidiurnal variances are only 0.32 and 0.34 of their true values, respectively. In other words, the altimeter underestimates the magnitude of the nonstationary and total semidiurnal variances by 68% and 66% respectively on average. Additionally, the SNVF is biased low by a factor of 0.92.

446 The spatial correlation of nonstationary tidal variance in the model with that
 447 inferred from altimetry suggests that the model is capturing a significant part of the
 448 interaction between baroclinic tides and the mesoscale circulation. A more compre-
 449 hensive evaluation of the nonstationary tides in HyCOM is challenged by the lack
 450 of global data sets with the temporal resolution and duration necessary to resolve
 451 tidal variability. Future validation efforts might consider comparison of the rates of
 452 water mass transformation and mixing driven by the dissipation of the internal tide.
 453 Although this is a higher order quantity further removed from the tidal forcing and
 454 air-sea exchange, the integrative nature of water mass properties might make them
 455 straightforward to compare between model output and in-situ data.

456 Acronyms

457 **HyCOM** HYbrid Coordinate Ocean Model

458 **MITgcm** Massachusetts Institute of Technology general circulation model

459 **GFDL** Geophysical Fluid Dynamics Laboratory

460 **GOLD** Generalized Ocean Layered Dynamics

461 **SWOT** Surface Water and Ocean Topography

462 **SSH** sea surface height

463 **SNVF** semidiurnal nonstationary variance fraction

464 Acknowledgments

465 The HyCOM outputs used in this study were obtained under the FY09-11 De-
 466 partment of Defense HPC Challenge Project Eddy Resolving Global Ocean Prediction
 467 including Tides and was provided by JFS (Shriver et al., 2012). The satellite altimeter
 468 data used in this study was extracted from the RADAR Altimetry Database System
 469 (RADS; <http://rads.tudelft.nl/rads/rads.shtml>) and processed by EDZ (Zaron,
 470 2017).

471 ADN, BKA, JFS, MCB, JGR, and ACS are grateful for support from NASA
 472 grants NNX17AH55G and NNX16AH79G as well as Office of Naval Research grant
 473 N00014-15-1-2288. EDZ acknowledged funding provided by the NASA award NNX16AH88G.
 474 ACS acknowledges funding provided by the NASA Earth and Space Science Fellowship
 475 grant NNX16AO23H. BKA and ACS acknowledge funding by the University of Michi-
 476 gan Associate Professor Support Fund, supported by the Margaret and Herman Sokol
 477 Faculty Awards. This NRL contribution NRL/JA/7320-19-4560 has been approved
 478 for public release.

479 The authors would also like to thank the two anonymous reviewers for their help
 480 in strengthening this paper.

481 References

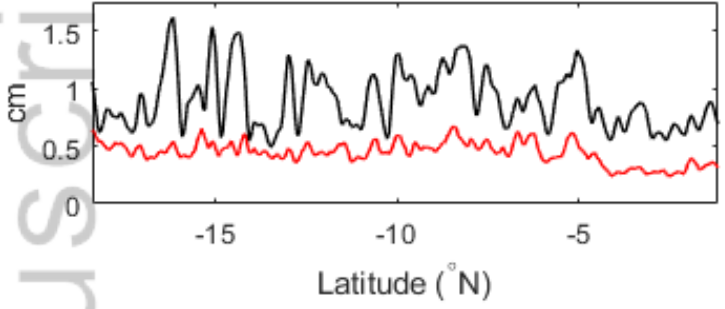
- 482 Ansong, J. K., Arbic, B. K., Alford, M. H., Buijsman, M. C., Shriver, J. F., Zhao,
 483 Z., . . . Zamudio, L. (2017). Semidiurnal internal tide energy fluxes and their
 484 variability in a global ocean model and moored observations. *Journal of Geo-*
 485 *physical Research: Oceans*, 122(3), 1882-1900. doi: 10.1002/2016JC012184
- 486 Ansong, J. K., Arbic, B. K., Buijsman, M. C., Richman, J. G., Shriver, J. F., &
 487 Wallcraft, A. J. (2015). Indirect evidence for substantial damping of low-mode
 488 internal tides in the open ocean. *J. Geophys. Res. Oceans*, 120, 6057-6071.
 489 doi: 10.1002/2015JC010998
- 490 Arbic, B., et al. (2018). A primer on global internal tide and internal gravity wave
 491 continuum modeling in HyCOM and MITgcm. In E. Chassignet, A. Pascual,

- 492 J. Tintore, & J. Verron (Eds.), *New Frontiers in Operational Oceanography*.
 493 GODAE OceanView.
- 494 Arbic, B. K., Richman, J. G., Timko, P. G., Metzger, E., & Wallcraft, A. J. (2012).
 495 Global modeling of internal tides within an eddying ocean general circulation
 496 model. *Oceanography*, 25(2), 20–29. doi: 10.5670/oceanog.2012.38
- 497 Arbic, B. K., Wallcraft, A. J., & Metzger, E. J. (2010). Concurrent simulation of the
 498 eddying general circulation and tides in a global ocean model. *Ocean Modell.*,
 499 32, 175–187. doi: 10.1016/j.ocemod.2010.01.007
- 500 Benada, J. R. (1997). *PO.DAAC Merged GDR (TOPEX/POSEIDON) Genera-*
 501 *tion B User's Handbook*. Retrieved from `\url{ftp://podaac.jpl.nasa.gov/`
 502 `allData/topex/L2/mgdrb/docs/uhmgdrb/html/usr_toc.htm}`
- 503 Buijsman, M. C., Arbic, B. K., Richman, J. G., Shriver, J. F., Wallcraft, A. J.,
 504 & Zamudio, L. (2017). Semidiurnal internal tide incoherence in the
 505 Equatorial Pacific. *J. Geophys. Res. Oceans*, 122, 5286–5305. doi:
 506 10.1002/2016JC012590
- 507 Colosi, J. A., & Munk, W. (2006). Tales of the venerable honolulu tide gauge. *Jour-*
 508 *nal of Physical Oceanography*, 36(6), 967–996. doi: 10.1175/JPO2876.1
- 509 Duda, T. F., Collis, J. M., Lin, Y.-T., Newhall, A. E., Lynch, J. F., & DeFerrari,
 510 H. A. (2012). Horizontal coherence of low-frequency fixed-path sound in a con-
 511 tinental shelf region with internal-wave activity. *The Journal of the Acoustical*
 512 *Society of America*, 131(2), 1782–1797. doi: 10.1121/1.3666003
- 513 Dunphy, M., & Lamb, K. G. (2014). Focusing and vertical mode scattering of the
 514 first mode internal tide by mesoscale eddy interaction. *Journal of Geophysical*
 515 *Research: Oceans*, 119(1), 523–536. doi: 10.1002/2013JC009293
- 516 Dunphy, M., Ponte, A. L., Klein, P., & Le Gentil, S. (2017). Low-mode internal tide
 517 propagation in a turbulent eddy field. *J. Phys. Oceanogr.*, 47, 649–665. doi: 10
 518 .1175/JPO-D-16-0099.1
- 519 Elipot, S., Lumpkin, R., Perez, R. C., Lilly, J. M., Early, J. J., & Sykulski, A. M.
 520 (2016). A global surface drifter data set at hourly resolution. *J. Geophys. Res.*
 521 *Oceans*, 65(1), 29–50.
- 522 Fu, L.-L., Alsdorf, D., Morrow, R., Rodrigues, E., & Mognard, N. (2012). SWOT:
 523 The Surface Water and Ocean Topography Mission - wide-swath altimetric
 524 measurement of water elevation on Earth. *JPL Publication*, 12(5). Retrieved
 525 from `http://swot.jpl.nasa.gov/files/SWOT_MSD_final-3-26-12.pdf`
- 526 Kelly, S. M., & Lermusiaux, P. F. J. (2016). Internal-tide interactions with the gulf
 527 stream and middle atlantic bight shelfbreak front. *J. Geophys. Res. Oceans*,
 528 121(8), 6271–6294. doi: 10.1002/2016JC011639
- 529 Kelly, S. M., Lermusiaux, P. F. J., Duda, T. F., & Haley, P. J. (2016). A coupled-
 530 mode shallow-water model for tidal analysis: Internal tide reflection and
 531 refraction by the Gulf Stream. *J. Phys. Oceanogr.*, 46, 3661–3679. doi:
 532 10.1175/JPO-D-16-0018.1
- 533 Kelly, S. M., Nash, J. D., & Kunze, E. (2010). Internal-tide energy over topography.
 534 *J. Geophys. Res. Oceans*, 115(C06014). doi: 10.1029/2009JC005618
- 535 Klymak, J. M., Simmons, H. L., Braznikov, D., Kelly, S., MacKinnon, J. A., Alford,
 536 M. H., ... Nash, J. D. (2016). Reflection of linear internal tides from realistic
 537 topography: The tasman continental slope. *J. Phys. Oceanogr.*, 46, 3321–3337.
 538 doi: 10.1175/JPO-D-16-0061.1
- 539 Luecke, C. A., Arbic, B. K., Bassette, S. L., Richman, J. G., Shriver, J. F., Alford,
 540 M. H., ... Wallcraft, A. J. (2017). The global mesoscale eddy available poten-
 541 tial energy field in models and observations. *Journal of Geophysical Research:*
 542 *Oceans*, 122(11), 9126–9143. doi: 10.1002/2017JC013136
- 543 Madec, G. (2008). *NEMO ocean engine*. Note du Pôle de modélisation, Institut
 544 Pierre-Simon Laplace (IPSL), France, No 27, ISSN No 1288-1619.
- 545 Müller, M., Cherniawsky, J. Y., Foreman, M. G. G., & von Storch, J.-S. (2012).
 546 Global M_2 internal tide and its seasonal variability from high resolution

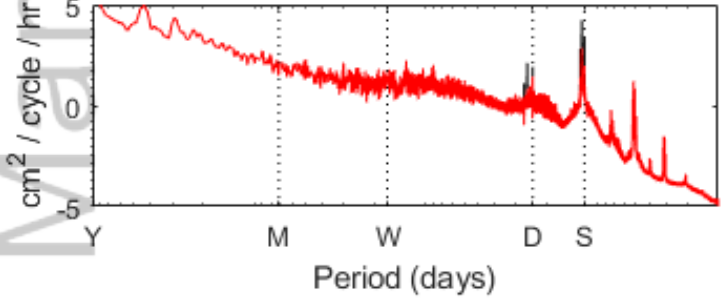
- 547 ocean circulation and tide modeling. *Geophys. Res. Lett.*, *39*(L19607). doi:
548 10.1029/2012GL053320
- 549 Ngodok, H. E., Souopgui, I., Wallcraft, A. J., Richman, J. G., & Shriver, J. F.
550 (2016). On improving the accuracy of the M₂ barotropic tides embedded in a
551 high-resolution global ocean circulation model. *Ocean Modell.*, *97*, 16–26. doi:
552 10.1016/j.ocemod.2015.10.011
- 553 Pujol, M.-I., Faugère, Y., Taburet, G., Dupuy, S., Pelloquin, C., Ablain, M., & Pi-
554 cot, N. (2016). DUACS DT2014: the new multi-mission altimeter data set
555 reprocessed over 20 years. *Ocean Science*, *12*(5), 1067–1090. Retrieved from
556 <https://www.ocean-sci.net/12/1067/2016/> doi: 10.5194/os-12-1067-2016
- 557 Ray, R. D. (1998). Spectral analysis of highly aliased sea-level signals. *J. Geophys.*
558 *Res. Oceans*, *103*(C11), 24991–25003. doi: 10.1029/98JC02545
- 559 Ray, R. D., & Mitchum, G. T. (1996). Surface manifestation of internal tides gener-
560 ated near Hawaii. *Geophys. Res. Lett.*, *23*(16), 2101–2104. doi: 10.1029/
561 96GL02050
- 562 Ray, R. D., & Mitchum, G. T. (1997). Surface manifestation of internal tides in the
563 deep ocean: Observations from altimetry and tide gauges. *Prog. in Ocean.*, *40*,
564 135–162. doi: 10.1016/S0079-6611(97)00025-6
- 565 Ray, R. D., & Zaron, E. D. (2011). Non-stationary internal tides observed
566 with satellite altimetry. *Geophys. Res. Lett.*, *38*(L17609). doi: 10.1029/
567 2011GL048617
- 568 Ray, R. D., & Zaron, E. D. (2016). M₂ internal tides and their observed wavenum-
569 ber spectra from satellite altimetry. *J. Phys. Ocean.*, *46*, 3–22. doi: 10.1175/
570 JPO-D-15-0065.1
- 571 Richman, J. G., Arbic, B. K., Shriver, J. F., Metzger, E. J., & Wallcraft, A. J.
572 (2012). Inferring dynamics from the wavenumber spectra of an eddying global
573 ocean model with embedded tides. *J. Geophys. Res.*, *117*(C12012). doi:
574 10.1029/2012JC008364
- 575 Rocha, C. B., Chereskin, T. K., Gille, S. T., & Menemenlis, D. (2016). Mesoscale to
576 submesoscale wavenumber spectra in Drake Passage. *J. Phys. Ocean.*, *46*, 601–
577 620. doi: 10.1175/JPO-D-15-0087.1
- 578 Rocha, C. B., Gille, S. T., Chereskin, T. K., & Menemenlis, D. (2016). Seasonal-
579 ity of submesoscale dynamics in the Kuroshio Extension. *Geophys. Res. Lett.*,
580 *43*(11), 304–311. doi: 10.1002/2016GL071349
- 581 Savage, A. C., Arbic, B. K., Richman, J. G., Shriver, J. F., Alford, M. H., Buijs-
582 man, M. C., ... Zamudio, L. (2017). Frequency content of sea surface height
583 variability from internal gravity waves to mesoscale eddies. *J. Geophys. Res.*
584 *Oceans*, *122*, 2519–2538. doi: 10.1002/2016JC012331
- 585 Shriver, J. F., Arbic, B. K., Richman, J. G., Ray, R. D., Metzger, E. J., Wallcraft,
586 A. J., & Timko, P. G. (2012). An evaluation of the barotropic and internal
587 tides in a high-resolution global ocean circulation model. *J. Geophys. Res.*
588 *Oceans*, *117*(C10024). doi: 10.1029/2012JC008170
- 589 Thoppil, P. G., Richman, J. G., & Hogan, P. J. (2011). Energetics of a global ocean
590 circulation model compared to observations. *Geophysical Research Letters*,
591 *38*(15). doi: 10.1029/2011GL048347
- 592 Timko, P. G., Arbic, B. K., Richman, J. G., Scott, R. B., Metzger, E. J., & Wall-
593 craft, A. J. (2012). Skill tests of three-dimensional tidal currents in a global
594 ocean model: A look at the North Atlantic. *J. Geophys. Res.*, *117*(C08014).
595 doi: 10.1029/2011JC007617
- 596 Timko, P. G., Arbic, B. K., Richman, J. G., Scott, R. B., Metzger, E. J., & Wall-
597 craft, A. J. (2013). Skill testing a three-dimensional global tide model to
598 historical current meter records. *J. Geophys. Res. Oceans*, *118*, 6914–6933.
599 doi: 10.1002/2013JC009071
- 600 Waterhouse, A. F., MacKinnon, J. A., Nash, J. D., Alford, M. H., Kunze, E., Sim-
601 mons, H. L., ... Lee, C. M. (2014). Global patterns of diapycnal mixing

- 602 from measurements of the turbulent dissipation rate. *J. Phys. Ocean.*, *44*(7),
603 1854–1872. doi: 10.1175/JPO-D-13-0104.1
- 604 Zaron, E. D. (2015). Non-stationary internal tides inferred from dual-satellite al-
605 timetry. *J. Phys. Oceanogr.*, *45*(9), 2239–2246.
- 606 Zaron, E. D. (2017). Mapping the nonstationary internal tide with satellite altime-
607 try. *J. Geophys. Res. Oceans*, *122*, 539–554. doi: 10.1002/2016JC012487
- 608 Zhao, Z., Alford, M. H., Garton, J. B., Rainville, L., & Simmons, H. L. (2016).
609 Global observations of open-ocean mode-1 M_2 internal tides. *J. Phys. Ocean.*,
610 *46*, 1657–1684. doi: 10.1175/JPO-D-15-0105.1
- 611 Zhou, X.-H., Wang, D.-P., & Chen, D. (2015). Validating satellite altimeter mea-
612 surements of internal tides with long-term TAO/TRITON buoy observations
613 at 2°S–156°E. *Geophys. Res. Lett.*, *42*.

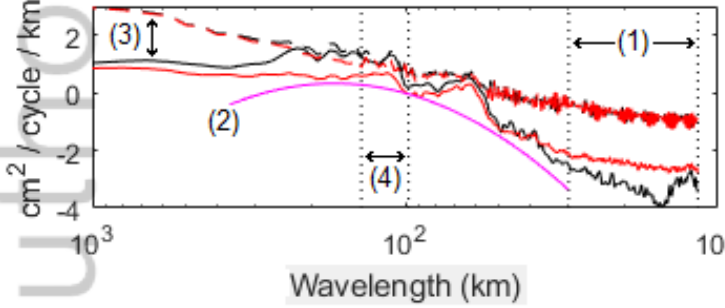
Along-track RMS SSH



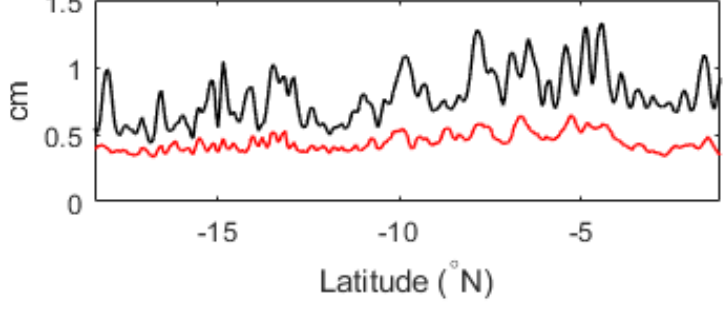
Mean F-Space PSD



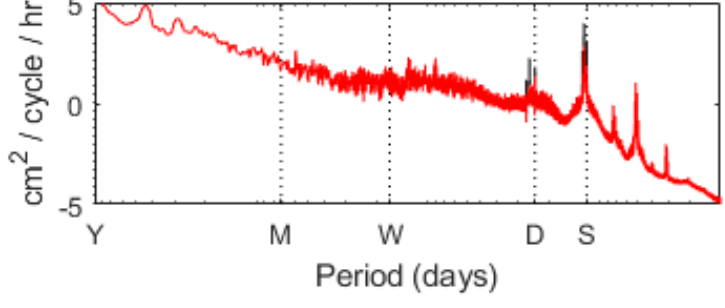
Mean K-Space PSD



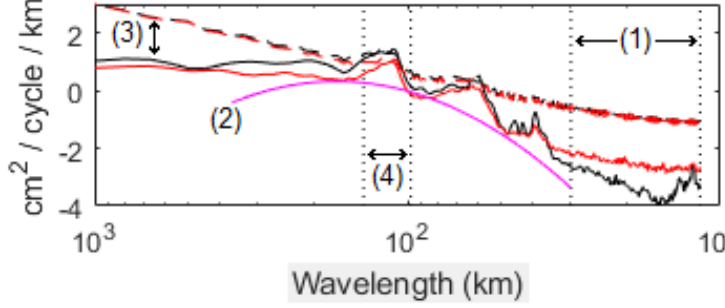
Along-track RMS SSH



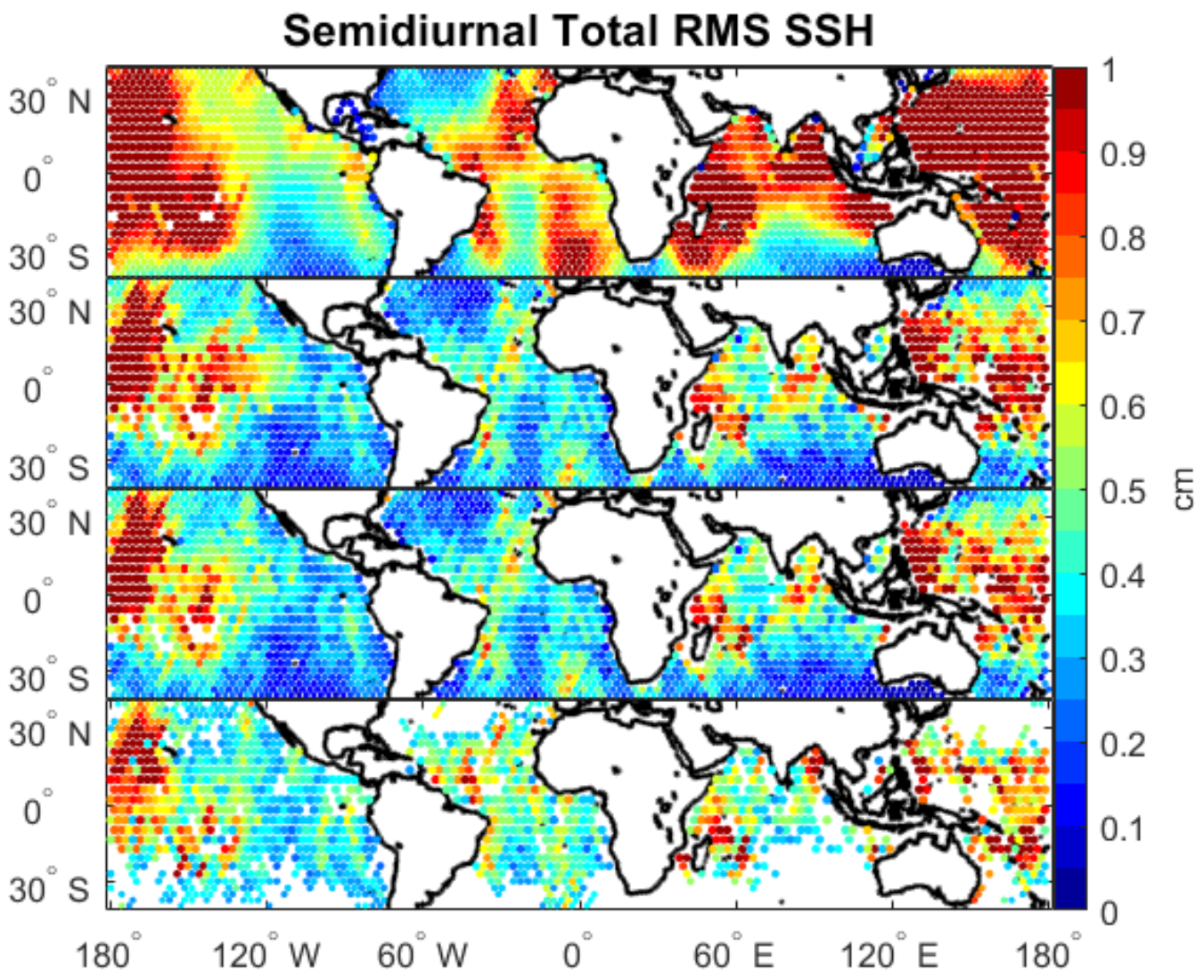
Mean F-Space PSD



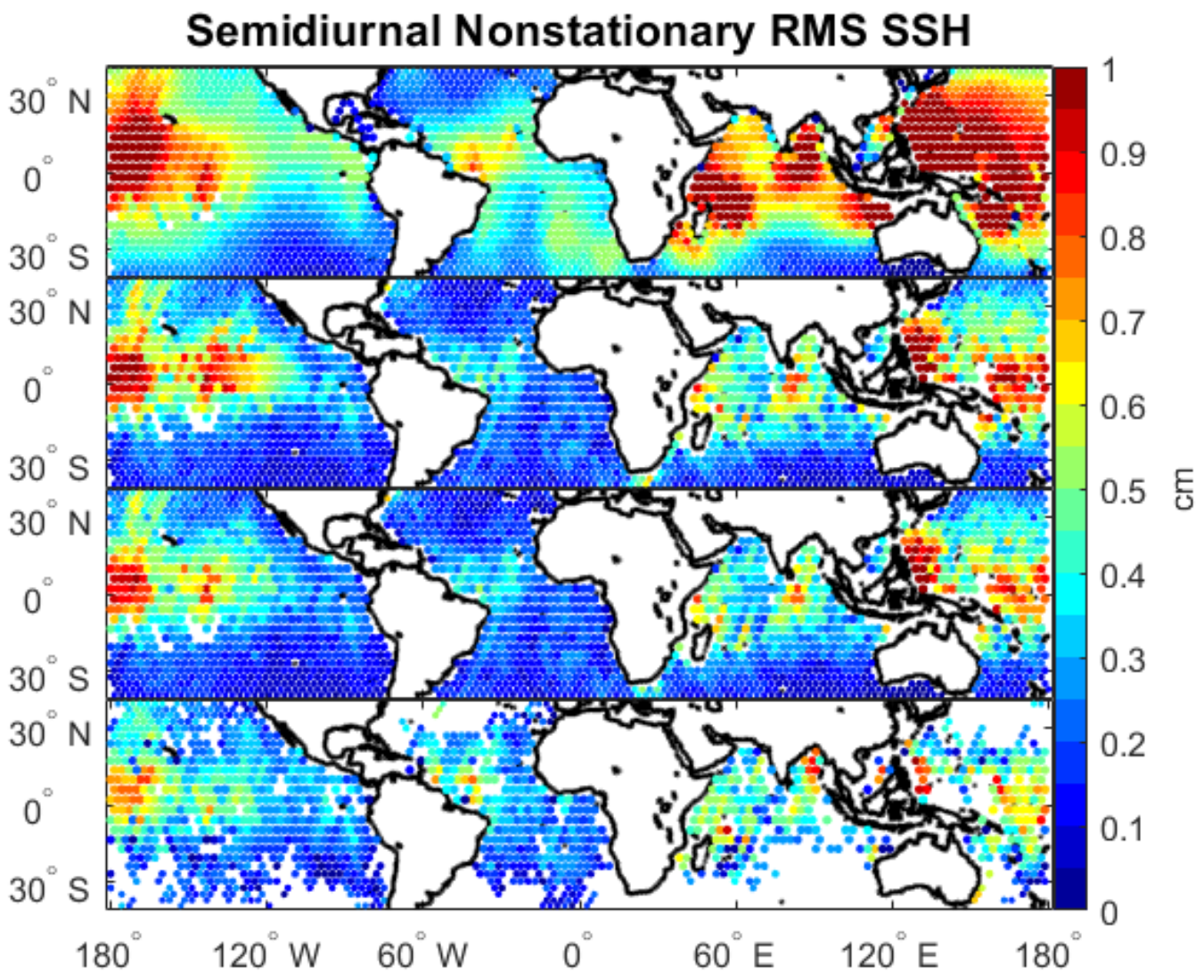
Mean K-Space PSD



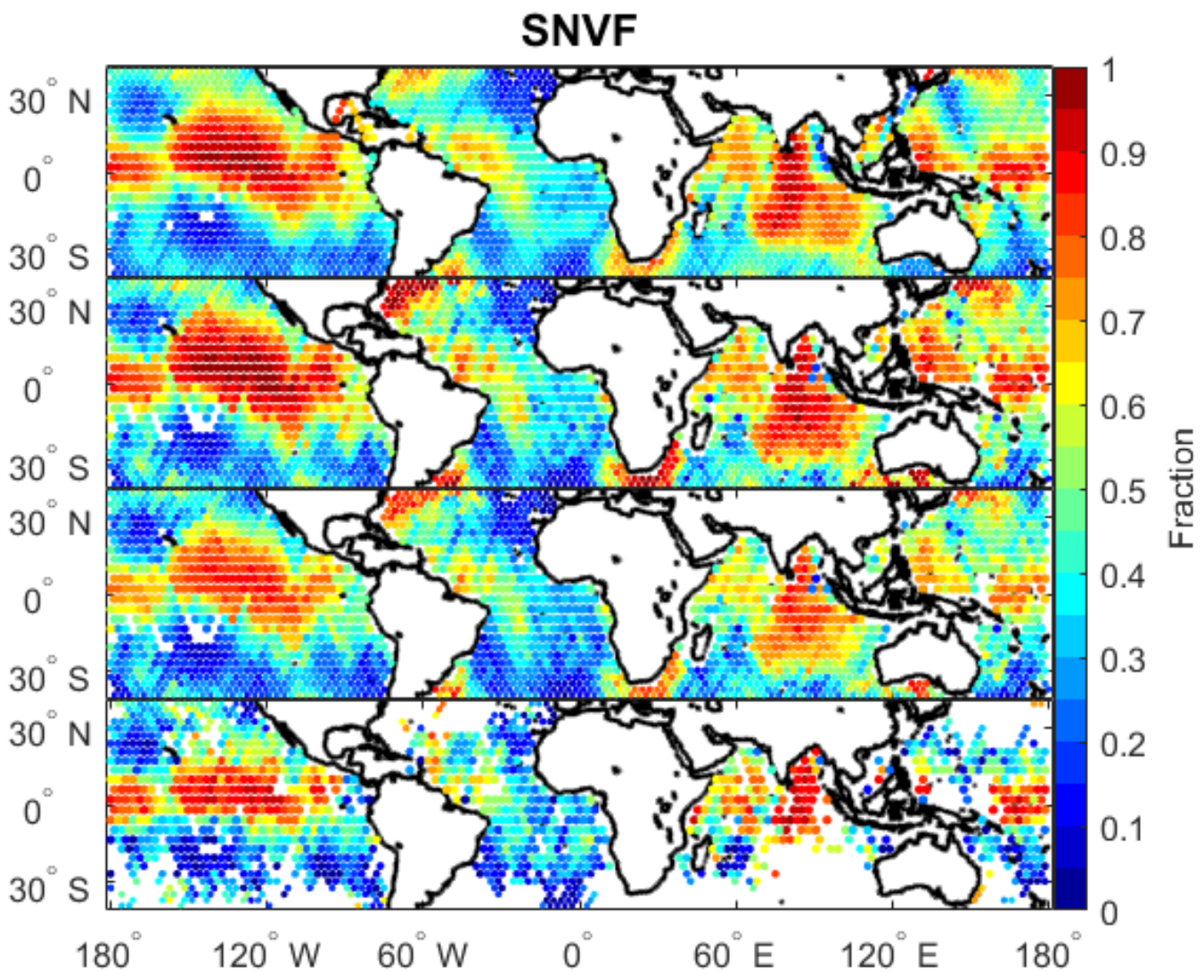
2018JC014737-f01-z-.png



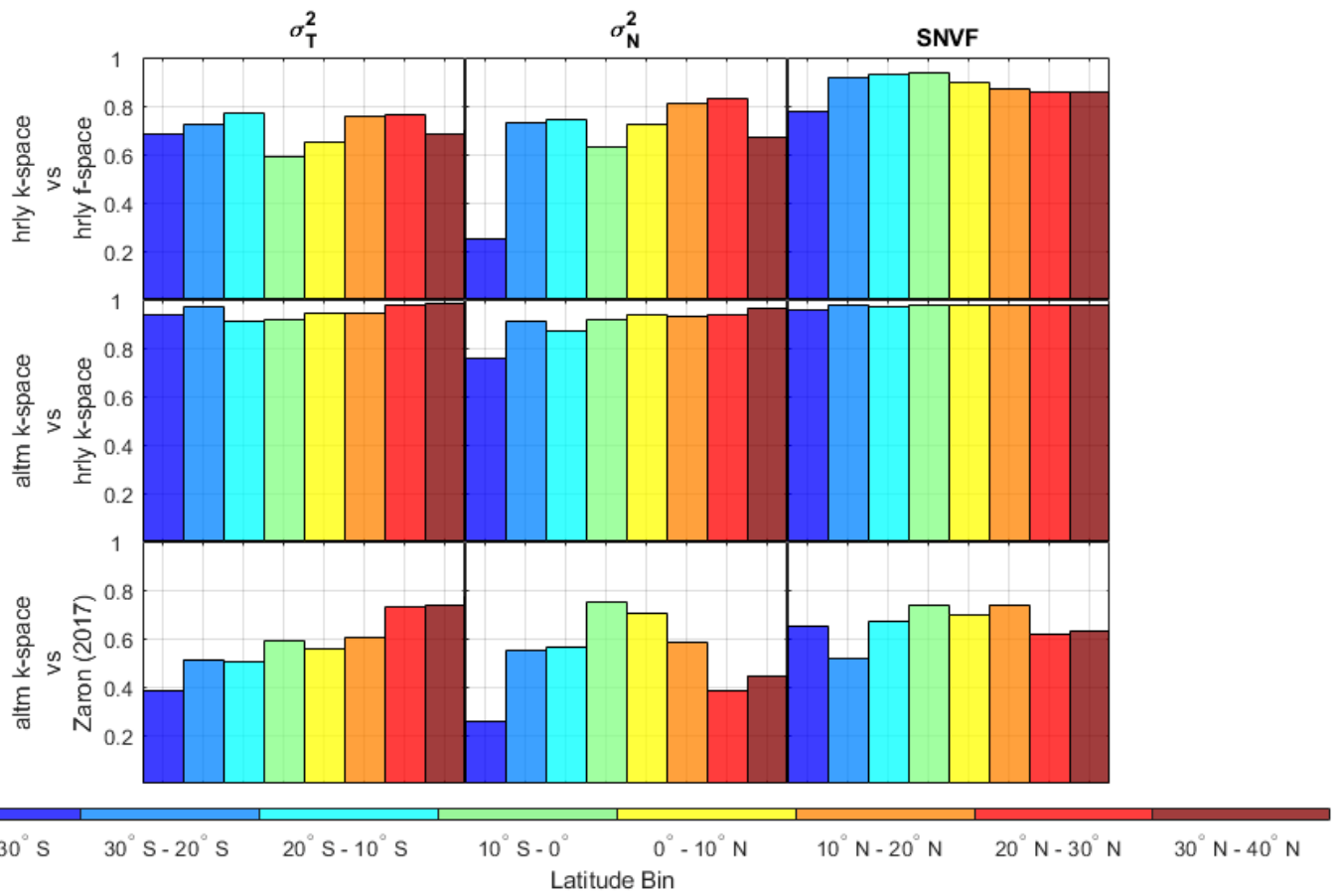
2018JC014737-f02-z-.png



2018JC014737-f03-z-.png



2018JC014737-f04-z-.png



2018JC014737-f05-z-.png